Collective stresses drive competition between monolayers of normal and Ras-transformed cells

Sarah Moitrier, Carles Blanch-Mercader, Simon Garcia, Kristina Sliogeryte, Tobias Martin, Jacques H. Camonis, Philippe Marcq, Pascal Silberzan, Isabelle Bonnet

Cite this: DOI: 10.1039/xxxxxxxxxx

Collective stresses drive competition between monolayers of normal and Ras-transformed cells†

Sarah Moitrier[abc‡], Carles Blanch-Mercader[d‡], Simon Garcia[abc], Kristina Sliogeryte[abc], Tobias Martin[abc], Jacques Camonis[ef], Philippe Marcq[ab*], Pascal Silberzan[abc] and Isabelle Bonnet[abc*]

Received Date
Accepted Date

DOI: 10.1039/xxxxxxxxxx

www.rsc.org/journalname

We study the competition for space between two cell lines that differ only in the expression of the Ras oncogene. The two cell populations are initially separated and set to migrate antagonistically towards an in-between stripe of free substrate. After contact, an interface moves towards the population of normal cells. We interpret the velocity and traction force data taken before and after contact thanks to a hydrodynamic description of collectively migrating cohesive cell sheets. The kinematics of cells, before and after contact, allows us to estimate the relative material parameters for both cell lines. As predicted by the model, the transformed cell population with larger collective stresses pushes the wild type cell population.

1 Introduction

Living organisms are composed of several tissues where cells continuously interact and compete for resources and space to ensure tissue cohesion and functionality[1–4]. Competitive interactions lead to the elimination of non-optimal cells and are crucial to maintain tissue integrity, homeostasis and function. Tissue organization is extremely stable but can be compromised in pathological situations, for instance in the case of tumor proliferation, where competitive cell interactions may also play a role[5]. Strikingly, it has indeed been proposed that precancerous cells could act as supercompetitors killing surrounding cells to make room for themselves[6]. Conversely, it has been observed that isolated cells either carrying tumor-promoting mutations[7–9] or deprived of tumor-suppressor genes[10], are eliminated from the wild type tissue. Importantly, the properties of entire groups of cells go beyond the sum of those of individual cells. A comprehensive understanding of these effects requires to integrate cell-cell interactions over tissue scales.

Recently, confrontation assays between antagonistically migrating cell sheets have been used[11–14] to study the interactions between normal and GFP-Ras^{V12} MDCK cells[12]. When Ras^{V12} and normal cells meet, the Ras^{V12} cells collapse and are displaced backwards, while normal cells continue to migrate forward. This displacement of the interface does not rely on the classical principle of contact inhibition of locomotion. From a biological point of view, it has been attributed to an ephrin-dependent mechanism: normal cells detect transformed Ras^{V12} cells through interactions between ephrin-A and its receptor EphA2. Using similar confrontation assays between two cell types expressing the EphB2 receptor and its ligand ephrinB1, it has been further shown that the repulsive interactions between two cell types drives cell segregation and border sharpening more efficiently than a low level of heterotypic adhesion[13]. The mechanical interactions between these two populations may lead to oscillatory traction force patterns, which pull cell-substrate adhesions away from the border, and may trigger deformation waves, generated at the interface between the two cell types and propagating across the monolayers[14]. The biomechanical determinants of dominance of a given cell population over another one remain unclear, as different theoretical descriptions of cell competition rely on differences in proliferation rates[15], in cell motilities[16,17], or predator-prey interactions[18].

In this work, we investigate the mechanisms of competitive cell interactions between normal and precancerous Human Embryonic Kidney (HEK) cell assemblies. In particular, we assess the invasive capacity of oncogene-bearing cells by adapting the classical wound healing assay[19] to an antagonistic migration assay (AMA) of two cell populations[11–14]. This approach holds the advantage of creating an interface between two cell populations in a reproducible way. Each cell type is seeded into one of the compartments of a cell culture insert so as to be initially separated by a gap. When the culture insert is removed, cells migrate to close the gap, and facing cells eventually meet. Later, it is observed that the *transformed* cell sheet penetrates the spatial domain occupied

[a] *Laboratoire Physico Chimie Curie, Institut Curie, PSL Research University, CNRS UMR168, 75005 Paris, France*
[b] *Sorbonne Université, 75005, Paris, France*
[c] *Équipe labellisée Ligue Contre le Cancer*
[d] *Université de Genève, Geneva, Switzerland*
[e] *Institut Curie, PSL Research University, 75005 Paris, France*
[f] *ART group, Inserm U830, 75005 Paris, France*
‡ These authors contributed equally to this work
* *E-mail: isabelle.bonnet@curie.fr; philippe.marcq@curie.fr*
† Electronic Supplementary Information (ESI) available: [details of any supplementary information available should be included here]. See DOI: 10.1039/b000000x/

by the wild type cell sheet and displaces it backwards. We adapt a biophysical model previously introduced[20] to describe the early dynamics of expansion of a single cell sheet into cell-free space and extract mechanical parameter values. Comparing theoretical predictions with experimental data, we show that differences in the amplitude of collective stresses developed at the free edges of the two independent migrating monolayers explain the displacement of the wild type cell population by the transformed cell sheet.

2 Materials and methods

2.1 Cell culture

Human Embryonic Kidney cell lines have been immortalized by ectopic expression of large-T and hTERT genes: the HEK-HT cells[21]. From now on, we refer to these cells as "HEK cells". In this work, we use the two following cell lines:

- HEK-GFP: a variant transduced to globally express the green fluorescent protein GFP, referred to below as the “wild type” or “normal” cell line (HEK wt);
- HEK-Ras-mCherry: a cell line carrying the H-RAS^{G12V} mutation, and transduced to globally express the fluorescent protein mCherry, referred to below as the “Ras” or “transformed” cell line (HEK Ras).

Cells were cultured in Dulbecco’s Modified Eagle’s Medium (DMEM GlutaMAX, Gibco) supplemented with penicillin-streptomycin (Gibco) and fetal bovine serum (FBS, Gibco) - respectively 1% and 10% vol/vol - at 37°C, 5% CO_2 and 95% relative humidity. The medium was also supplemented with selection antibiotics according to cell line’s specific resistance, namely with hygromycin B (100 μg/mL, Gibco) and geneticin (400 μg/mL, Gibco) for both cell lines, and with additional puromycin (0.5 μg/mL, Gibco) for the Ras cell line.

2.2 Population doubling time

For the estimation of the population doubling time τ_d, cells from each cell line were seeded in 8 wells of a plastic bottom 24-well plate. Twice a day, for 4 consecutive days, the cells from one well were resuspended using Trypsin-EDTA (Gibco) and counted in a given volume using a KOVA Glasstic Slide 10 with Grids (KOVA). Assuming that the number n of cells as a function of time after seeding follows $n(t) = n_0 2^{t/\tau_d}$, where n_0 denotes the initial cell number, we deduce an estimation from the slope of the graph $n = f(t)$ with semi-logarithmic axes since $\log(n) = \log(n_0) + t\log(2)/\tau_d$. We found $\tau_d^{\mathrm{wt}} = 16 \pm 3$h and $\tau_d^{\mathrm{Ras}} = 16 \pm 1$h, see Fig. S1.

2.3 Immunostaining

Cells were fixed using 4% paraformaldehyde (PFA, Electron Microscopy Science, ref. 15710) for 20 min. Samples were then washed three times in phosphate buffer saline (PBS). For permeabilization, cells were treated with 0.5% Triton X-100 for 10 min, followed with three rinsing steps in PBS. Non-specific binding was blocked by incubating in 3% bovine serum albumine (BSA, Sigma) in PBS for 30 min. Samples were then incubated with primary antibody N-cadherin rabbit (7939, Santa Cruz) diluted 1:200 and E-cadherin mouse (610181, BD biosciences) diluted 1:100 in PBS with 0.5% BSA for 60 min. After incubation, samples were washed three times in PBS and incubated in secondary antibody Alexa Fluor 488 chicken anti-rabbit and Alexa Fluor 546 goat anti-mouse (respectively A21441 and A11003, both from Invitrogen) diluted in 1:1000. DNA binding dye (DAPI, ThermoFisher) was added at 1 μg.mL^{-1} in PBS with 0.5% BSA for 60 min. The samples were washed again in PBS and mounted with Prolong Gold reagent (Life technologies). Images were acquired with a Zeiss LSM NLO 880 confocal microscope using ZEN software. The final images are presented as the sum of Z-stacks. We used MDCK cells as a control for antibody validation.

2.4 Antagonistic migration assay

We used commercially available silicone-based Culture-Inserts 2 Well (Ibidi), whose outer dimensions are $9 \times 9\,\mathrm{mm}^2$. Each well covers a surface of $22\,\mathrm{mm}^2$. The insert was placed in 6-well glass bottom plates (IBL, Austria) and the cells were seeded at roughly 0.5 million cells/mL. The normal cell type was always seeded in the left compartment of the culture insert, while the transformed cells were seeded in the right compartment. Cells were left to incubate overnight until fully attached - then, the culture insert was removed, leaving a free space between the two monolayers, which could then migrate towards each other to close this gap.

The plane occupied by the cell sheets is described by cartesian coordinates, where x denotes the direction of migration, see Fig. 1. Initially, the two monolayers are set apart by a cell-free gap of width $\Delta x = |x_{\mathrm{initial}}^{\mathrm{wt}} - x_{\mathrm{initial}}^{\mathrm{Ras}}| \sim 400\,\mu$m. The removal of the barrier sets the reference time $t = 0$.

Time-lapse experiments were carried out using an 10x objective (HCX PL Fluotar, 0.3 Ph1, Leica) mounted on an DM-IRB inverted microscope (Leica) equipped with temperature, humidity, and CO_2 regulation (Life Imaging Services). The motorized stage (H117 motorized stage, Prior Scientific), and the image acquisition with a CCD camera (CoolSnap EZ (Photometrics) or Retiga 6000 (Qimaging)) were controlled using Metamorph software (Molecular Devices). The typical delay between successive images was 15 min. We followed the AMA during 3 days by acquiring images in three channels: phase contrast (all cells), GFP (HEK cells) and mCherry (HEK Ras cells). In this work, the analysis has been performed during the first 60 h after barrier removal, that is until the tissue becomes multilayered.

Custom-made ImageJ[22] macros were used to automatically process large numbers of images for stitching, merging channels and assembling movies. We have used green and magenta as false colours for GFP and mCherry signals.

2.5 Velocimetry

The velocity fields in the cell monolayers were analyzed by particle image velocimetry (PIV) using the MatPIV toolbox for Matlab (Mathworks), as previously described[23,24]. The window size was set to 16 pixels ($\sim 40\,\mu$m typically), with an overlap of 0.25. Sliding average over 1 h was performed.

Averaging the velocity fields along the y direction, we fitted ve-

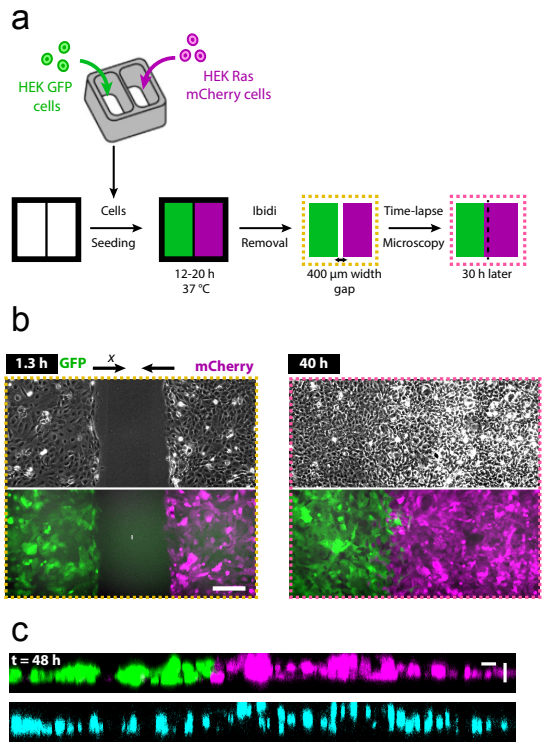

Fig. 1 Principle of the antagonistic migration assay. a: Schematics of the experimental procedure. The time reference $t = 0$ corresponds to insert removal. b- Left: initially, the two cell populations are separated by a cell-free gap of $\Delta x \sim 400\mu$m . Phase contrast (top) and fluorescence images (bottom) of the cell monolayers at $t = 1.3$ h. The cell populations migrate along the x axis in opposite directions. b- Right: gapless monolayer at $t = 40$ h. Scale bar: 200μm. c: Side view of the AMA at $t = 48$ h (not the same experiment as in b). Top: HEK-GFP cells (green) and HEK-Ras-mCherry cells (magenta). Bottom: Hoechst labelling (nuclei). Note that after fusion, the tissue remains monolayered. Scale bars: 25μm

locity profiles $v(x)$ with a single exponential function $\sim V\exp((x - L(t))/\lambda)$, where $L(t)$ is the position of the front at time t and it is determined by the position of the extrema of the measured velocity profiles. To improve accuracy of the measurement, the parameters V and λ were estimated from the first two moments of the velocity profiles, as it led to substantially smaller error bars than other fitting procedures. For instance, our estimates of parameters of the normal monolayer velocity profile read $\lambda^{\mathrm{wt}} = \int_{-\infty}^{L^{\mathrm{wt}}(t)}(L^{\mathrm{wt}}(t) - x)v(x)\mathrm{d}x/\int_{-\infty}^{L^{\mathrm{wt}}(t)} v(x)\mathrm{d}x$, $V^{\mathrm{wt}} = \int_{-\infty}^{L^{\mathrm{wt}}(t)} v(x)\mathrm{d}x/\lambda^{\mathrm{wt}}$. Similar expressions can be derived to estimate λ^{Ras} and V^{Ras}.

2.6 Traction Force Microscopy

We adapted the protocol from Tse and Engler[25]. First, we prepared "activated" coverslips : coverslips were cleaned in a plasma cleaner for 10 minutes, incubated in a solution of 3-aminopropyltrimethoxysilane (2% vol/vol in isopropanol, Sigma) for 10 minutes, and rinsed with distilled water. They were then incubated in glutaraldehyde (0.5% vol/vol in water, Sigma) for 30 minutes, and air dried. Independently, microscope glass slides were incubated in a solution of Fibronectin Bovine Protein (Gibco) in PBS at $25\,\mu$g/mL for 30 minutes, then left to air dry. We mixed a solution of 40% acrylamide (Bio-Rad) with a solution of 2% bis-acrylamide (Bio-Rad) in water, and added 1% (vol/vol) of fluorescent beads (FluoSpheres $0.2\,\mu$m dark red fluorescent 660/680, Life Technologies) in order to make a gel of $\sim$ 20kPa.

To start the polymerization of the gel, ammonium persulfate (1% vol/vol, Bio-Rad) and TEMED (1‰ vol/vol Bio-Rad) were added to the solution containing the beads and thoroughly mixed. Then $30\,\mu$L was applied on the fibronectin-coated slides, and activated coverslips were placed on top. This step, inspired by the deep-UV patterning technique[26], enabled us to directly coat the surface of the gel with fibronectin.

When the polymerization was complete, the sandwiched gel was immersed in PBS, and the coverslip bearing the gel was carefully detached. It was then incubated in culture medium for 45 minutes, at 37°C, before the cells were seeded on its surface, and left to adhere overnight. We finally used a POCmini-2 cell cultivation system (Pecon GmbH) for image acquisition under the microscope. The images were acquired as usual, with the added far red channel to image the beads. Reference images of the beads in the gel at rest were taken after trypsinization. Traction forces were computed using the Fiji plugins developed by Tseng *et al.*[27].

Note that TFM experiments are done on soft acrylamide gels, which are fibronectin-coated, while we generally carried out experiments on plain glass. However, experiments conducted on fibronectin-coated glass showed that fibronectin does not change the final outcome of the AMA, although it may affect its dynamics. The traction force measurements are acquired $t = 1$ h after barrier removal at uniform time intervals of 15 minutes. To improve the accuracy of our data, time averages are performed over time windows of 2.5 hours. We observe a relaxation of the spatial autocorrelation function of both components T_x and T_y of the traction force field, and estimate the traction force correlation lengths by the position at half-height of the autocorrelation function. For isolated cells, we measure both traction forces (see Fig. S2) and strain energy density. The latter is the strain energy divided by the cell area[28].

2.7 Statistical analysis

Statistical significance was quantified by p-values calculated by a Mann-Whitney U test. Different levels of significance are shown on the graphs: * p $\leq$ 0.1; ** p $\leq$ 0.05; *** p $\leq$ 0.01. p-values larger than 0.1 were considered not significant ('n.s').

2.8 Model

We briefly summarize here the model of an active viscous material proposed in Blanch-Mercader *et al.*[20] to describe the expansion of a planar cell sheet spreading in a direction defining the x axis, in the limit where the extension of the system along the y axis is much larger than along x. In this case, approximate translation invariance along y allows to treat the system in 1D along the x axis, by averaging all relevant fields over y. We denote $v(x,t)$, $p(x,t)$ and $\sigma(x,t)$ the x components of the velocity, polarity and stress fields. Within a continuum mechanics approach, the equa-

tions governing monolayer expansion into free space read:

$$\sigma = \eta\,\partial_x v, \tag{1}$$

$$\partial_x \sigma = \xi v - T_0 p, \tag{2}$$

$$0 = p - L_c^2\,\partial_x^2 p\,. \tag{3}$$

They respectively represent: (1) the constitutive equation for a viscous compressible fluid with viscosity η; (2) the force balance equation at low Reynolds number in the presence of both passive (friction coefficient ξ) and active (magnitude T_0) traction forces; and (3) the polarity equation in the quasi-static limit. The length L_c is the length scale over which the monolayer front is polarized and generates active traction forces.

In the case of a single monolayer located in the domain $x \le L(t)$ at time t, and expanding towards $x > 0$, the boundary conditions read:

$$\sigma(x = L(t), t) = 0, \tag{4}$$

$$p(x = L(t), t) = +1, \tag{5}$$

leading to the polarity profile ($x \le L(t)$):

$$p(x,t) = \exp\left(\frac{x - L(t)}{L_c}\right) \tag{6}$$

and to the velocity and stress profiles:

$$v(x,t) = \frac{v_{\text{front}}}{L_c - L_\eta}\left(L_c \exp\left(\frac{x-L(t)}{L_c}\right) - L_\eta \exp\left(\frac{x-L(t)}{L_\eta}\right)\right), \tag{7}$$

$$\sigma(x,t) = \frac{\eta v_{\text{front}}}{L_c - L_\eta}\left(\exp\left(\frac{x-L(t)}{L_c}\right) - \exp\left(\frac{x-L(t)}{L_\eta}\right)\right), \tag{8}$$

where

$$L_\eta = \sqrt{\eta/\xi} \tag{9}$$

is the hydrodynamic length and the velocity v_{front} of the moving front reads:

$$v_{\text{front}} = v(x = L(t), t) = \frac{T_0 L_c}{\xi(L_c + L_\eta)}\,. \tag{10}$$

This model can be generalized to describe the mechanical behavior of the gapless monolayer after fusion of the expanding normal and transformed cell sheets. With the geometry of Fig 1 in mind, we denote quantities pertaining to the transformed (respectively normal) cells with the index r (respectively l), occupying the domain defined by $x \ge L(t)$ (respectively $x \le L(t)$) at time t.

Eqs. (1-3) apply for each cell sheet, distinguished by a set of distinct parameters:

$$\sigma^{l,r} = \eta^{l,r}\,\partial_x v^{l,r}\,. \tag{11}$$

$$\partial_x \sigma^{l,r} = \xi^{l,r} v^{l,r} - T_0^{l,r} p^{l,r}, \tag{12}$$

$$0 = p^{l,r} - (L_c^{l,r})^2\,\partial_x^2 p^{l,r}\,. \tag{13}$$

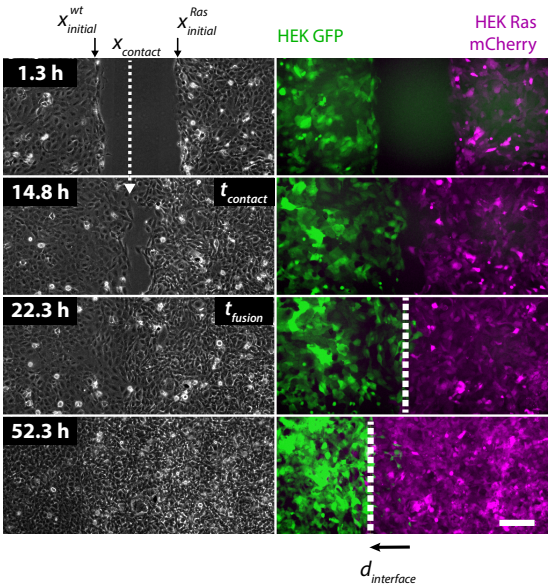

Fig. 2 Kinematics of the antagonistic migration assay between HEK-GFP (green) and HEK-Ras-mCherry (magenta) cells. Four time-points of a representative AMA. Phase contrast (left) and fluorescence images (right).The time reference $t = 0$ corresponds to the barrier's removal. From top to bottom: first time-point of the acquisition, t_{contact}, t_{fusion} and $t = 30$ h after the fusion. Note the backward migration of the HEK-GFP population after contact and fusion. We indicate $x^{\text{wt}}_{\text{initial}}$, $x^{\text{Ras}}_{\text{initial}}$, x_{contact} (white dashed line), as well as the displacement $d_{\text{interface}}$ of the interface within 30 h after t_{contact}. Scale bar: 200 μm.

The boundary conditions at the interface read:

$$\sigma^l(x = L(t), t) = \sigma^r(x = L(t), t), \tag{14}$$

$$v^l(x = L(t), t) = v^r(x = L(t), t), \tag{15}$$

$$p^l(x = L(t), t) = 1, \tag{16}$$

$$p^r(x = L(t), t) = -1\,. \tag{17}$$

An important assumption is that we ignore a possible repolarization of the cell sheets after a change of the direction of migration (16-17). Integration of the evolution equations (11-13) with boundary conditions (14-17) leads to the following expression of the interface velocity $v_{\text{interface}}$:

$$v_{\text{interface}} = v(x = L(t), t) = \frac{L_\eta^r \eta^l v^l_{\text{front}} - L_\eta^l \eta^r v^r_{\text{front}}}{L_\eta^l \eta^r + L_\eta^r \eta^l}, \tag{18}$$

with left and right front velocities $v^{l,r}_{\text{front}}$ obtained as above using (10) with l and r material parameters. Remarkably, the interface velocity can be rewritten as

$$v_{\text{interface}} = \frac{\sigma^l_{\text{front}} - \sigma^r_{\text{front}}}{\eta^r/L_\eta^r + \eta^l/L_\eta^l}, \tag{19}$$

upon defining

$$\sigma_{\text{front}} = \frac{\eta\, v_{\text{front}}}{L_\eta} = \frac{T_0 L_c L_\eta}{L_c + L_\eta}, \tag{20}$$

where the front stress σ_{front} can be interpreted as the maximum

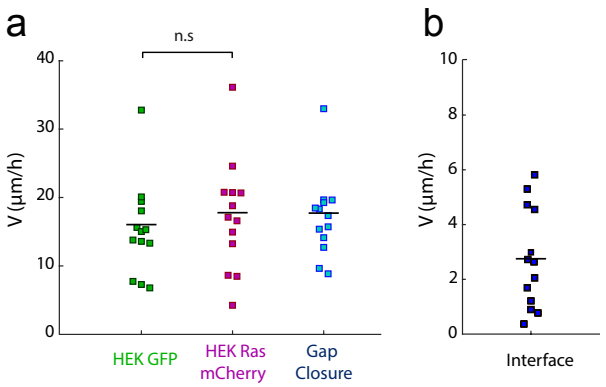

Fig. 3 Front velocities. a : velocities of the fronts of expanding cell sheets (HEK-GFP in green and HEK-Ras-mCherry in magenta) and of the gap closure. b: velocity of the interface between the two populations after the meeting. Horizontal black lines correspond to mean values.

stress value within a cell sheet whose boundary is clamped at a fixed position (see Appendix A). The direction of motion of the interface between two competing tissues, given by the sign of $\sigma^l_{\rm front} - \sigma^r_{\rm front}$, is determined by the collective stresses that build up at the fronts.

3 Results

3.1 Characterization of cell lines

The two HEK cell lines form monolayers in culture (see phase contrast images of Figs 1-2 + ESI movie). The Ras mutation does not affect the population doubling time of the cells since we found a doubling time of 16 ± 3 h for normal and 16 ± 1 h for transformed cells (Fig. S1).

We note that a confluent monolayer of transformed cells contains about twice as many cells as a confluent monolayer of normal cells for the same area. Indeed, isolated HEK normal cells are approximately twice as large as HEK Ras cells: we measured a mean area of $3100 \pm 1100\,\mu$m^2 and $1600 \pm 400\,\mu$m^2 for normal and transformed cells, respectively (Standard Deviation SD, $n = 14$).

In order to mechanically characterize the two cell lines, we first estimated the traction forces developed by isolated HEK cells on their substrate using traction force microscopy. We found that the mean traction force amplitude was larger for HEK wt cells compared to HEK Ras cells: 110 ± 32 Pa and 65 ± 29 Pa, respectively (SD, $n = 15$ and $n = 13$, Fig. S2). Since the two cell types differ in size, we also computed the strain energy density, and found that the strain energy density was about 3 times higher for wt cells compared to Ras cells: $3.5 \pm 2.1 \times 10^{-5}$ J.m^{-2} and $1.1 \pm 0.7 \times 10^{-5}$ J.m^{-2} (SD, $n = 15$ and $n = 13$, not shown). Such a decrease of traction forces upon the expression of H-Ras has been reported for isolated NIH3T3 fibroblasts[29].

Next, we analyzed the statistical properties of collective cell traction forces far from the margin, focusing on two windows of 0.6 mm $\times$ 3 mm on the leftmost region of HEK-GFP monolayers and on the rightmost region of HEK-Ras-mCherry monolayers (see Fig. 1). The leading edges were at least 700 μm away from the analyzed force data in these windows. Fig. S3,a shows that the distribution of force orientation was approximately uniform for both cell types, suggesting that both monolayer subsets were mechanically disconnected from the corresponding leading edges, and that possible traction force correlations occur over a length scale smaller than 700 μm. Fig. S3,b shows that normal cells exerted forces of amplitude 51 ± 6 Pa (SD, n=4), comparable to transformed cell forces 48 ± 3 (SD, n=4). Importantly, collective cell traction force behaviour could not be extrapolated from single cell traction forces.

3.2 Before contact, both monolayers migrate freely

Upon removal of the insert, the monolayers migrate toward each other, while spreading on the free surface. The phase contrast images allow us to extract the position $x_{\rm contact}$ of the first contact between the two opposite populations as well as the corresponding time $t_{\rm contact}$ (Fig 2 - 2$^{\rm nd}$ panel). We define a second characteristic time: $t_{\rm fusion}$ which is the time when the gap closes completely (Fig. 2- 3$^{\rm rd}$ panel). We observe that the two populations meet $t_{\rm contact} = 16.5 \pm 5.6$ h (SD, $n = 13$) after barrier removal, and that the gap closes completely within $t_{\rm fusion} = 27.9 \pm 6.3$ h (SD, $n = 13$). We define the average front velocity of each monolayer as: $v^{\rm wt,Ras}_{\rm front} = \frac{|x_{\rm contact} - x^{\rm wt,Ras}_{\rm initial}|}{t_{\rm contact}}$, where $x^{\rm wt,Ras}_{\rm initial}$ denotes the position of each cell front at $t = 0$ (Fig. 2). The normal and transformed monolayers migrate with similar front velocities: $v^{\rm wt}_{\rm front} = 16 \pm 5\,\mu$m h^{-1} and $v^{\rm Ras}_{\rm front} = 18 \pm 6\,\mu$m h^{-1} (SD, $n = 13$). We also measure the gap closure velocity, defined as $v^{\rm gap}_{\rm front} = \frac{\Delta x}{t_{\rm fusion}} = 18 \pm 5\,\mu$m h^{-1} (Fig. 3,a), consistent with the other definitions of the front velocity. We have checked that variations of the initial cell densities, and of the initial front velocities, of the two monolayers do not impact the behavior of the interface after the meeting.

The velocity fields were computed using PIV on the phase contrast images for $x < x_{\rm contact}$ and $t < t_{\rm contact}$. We note that the orientation of the velocity streamlines for the wild type cells is more uniform (Fig. S4). The normal population migrates in a more directed manner than the transformed one. We checked that the mean velocities along the y-direction are close to zero for the two populations.

3.3 Data analysis

For times before the first contact $t \leq t_{\rm contact}$, we analyze the velocity fields measured by PIV and the statistical properties of the traction force fields in the light of the theoretical framework given by Eqs. (1-3). As shown in Fig. 4a, the velocity profiles decay over a lengthscale λ of several hundred micrometers from a maximal value observed at the front. Further, the velocity profiles are in good agreement with a *single* exponential function $\sim \pm V \exp(\pm(x - L(t))/\lambda)$ (Fig. 4,a). For times $t_{\rm contact} - 2\,{\rm h} \leq t \leq t_{\rm contact}$, we checked that the fitting parameters (V, λ) remained constant within error bars (Fig. S5).

Cell traction force fields (T_x, T_y) display a rather noisy distribution in space without clear regular patterns (Fig. 5,a). We next focused on the statistical properties of collective cell traction forces including the free boundary, computing averages as explained above, but over wider windows of size 1.26 mm $\times$ 3 mm for each monolayer, which include their leading edges (see Characterization of cell lines). Upon averaging over the y-axis, we find

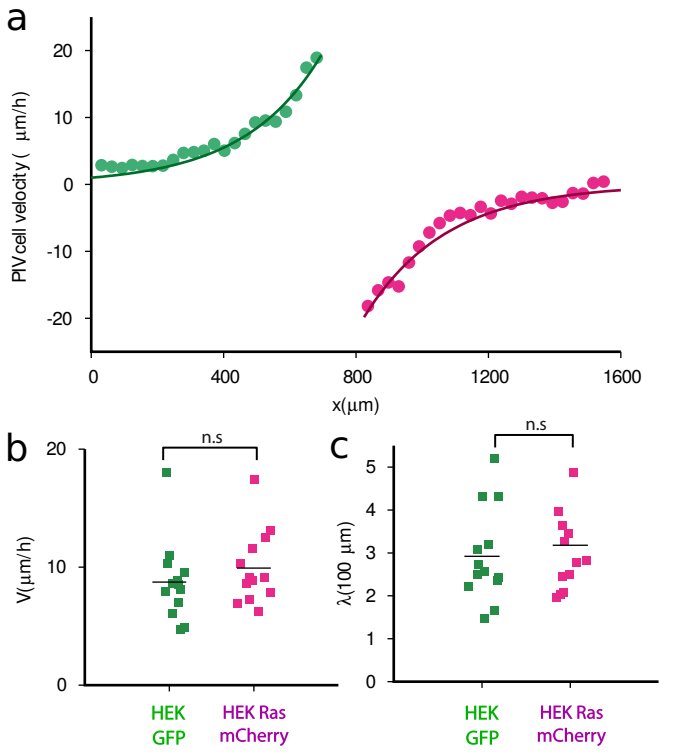

Fig. 4 Velocity profiles. a. Example of the AMA velocity profiles (dots) measured by PIV in the monolayers, $t = 6.75$ h. In this experiment $t_{\mathrm{contact}} = 8.5$ h. On the left hand side, the monolayer is composed of HEK-GFP cells (green dots) and on the right hand side, the monolayer is composed of HEK-Ras-mCherry cells (magenta dots). The green (resp. magenta) solid curve represents the best fit of the function $V^{\mathrm{wt}} \exp((x-L)/\lambda^{\mathrm{wt}})$ (resp. $-V^{\mathrm{Ras}} \exp(-(x-L)/\lambda^{\mathrm{Ras}})$), where L is the position of the front and (V, λ) are the fitting parameters. b. Set of fitted front velocities V. c. Set of fitted exponential decay lengths λ. Horizontal black lines correspond to mean values.

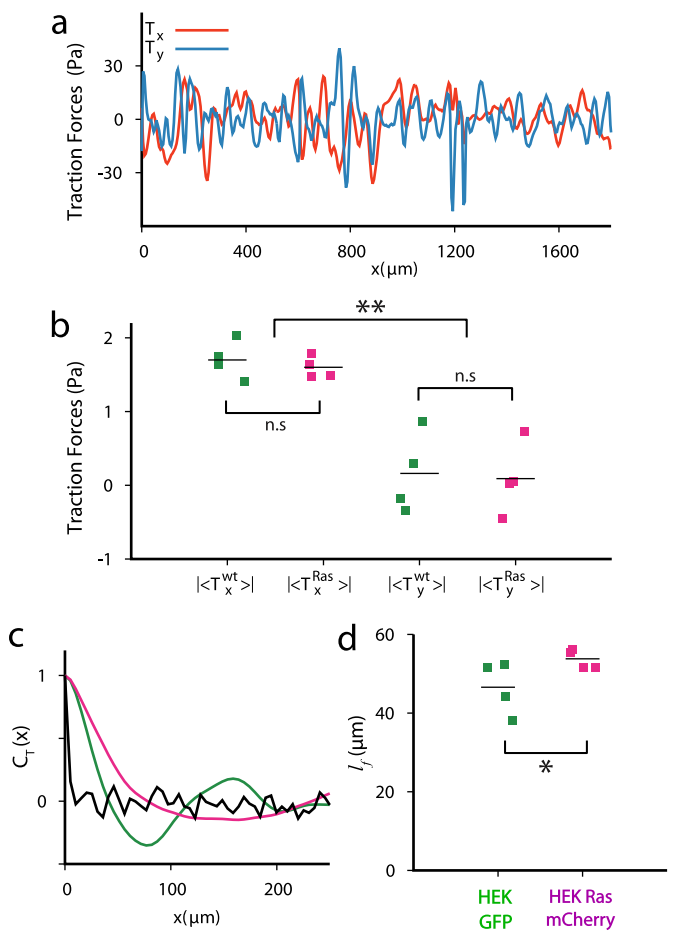

Fig. 5 Characteristic parameters of traction force fields. a. Traction force profiles 1 h after barrier removal. b. Mean traction force components $\langle T_x \rangle$ and $\langle T_y \rangle$ for HEK-GFP (green squares) and HEK-Ras-mCherry cells (magenta squares) cell monolayers. c. Autocorrelation functions of traction forces T_x for HEK (green) and HEK Ras (magenta). The black curve is the autocorrelation function of white noise for control. d. Correlation lengths of the x-component of traction forces T_x. All traction force data in the figure are averaged along the y direction, perpendicular to the direction of migration. Horizontal black lines correspond to mean values.

that $|\langle T_x \rangle^{\mathrm{Ras,wt}}| > |\langle T_y \rangle^{\mathrm{Ras,wt}}|$ (Fig. 5,b), suggesting that the mean traction forces approximately parallels the direction of migration x. Unlike for assemblies of randomly oriented force dipoles, the mean traction forces $\langle T_x \rangle$ are non-vanishing for both cell types (Fig. 5,b), indicating that these cells coordinate forces over distances that are large compared to the typical cell size, as found for epithelial cells[30]. We denote l_f the decay length of the autocorrelation function of the x component of the traction force (Fig. 5,c). We find that transformed cells coordinate force over longer distances $l_f^{\mathrm{Ras}} = 54 \pm 2\,\mu$m than normal cells $l_f^{\mathrm{wt}} = 47 \pm 7\,\mu$m (SD, $n = 4$) (Fig. 5,d).

Identifying l_f with L_c, the comparison of the typical length scale of velocity variations ($\sim 300\ \mu$m) with the correlation length of traction forces ($\sim 50\ \mu$m), suggests that monolayer spreading occurs in the theoretical limit $L_c \ll L_\eta$, that we assume from now on. In this limit, Eq. (7) reduces to a single exponential function $\sim V \exp((x - L(t))/\lambda)$, where V is identified with the front velocity v_{front} and λ with the hydrodynamic length L_η, while $\sigma_{\mathrm{front}} \approx T_0 L_c$ according to Eq. (20). We estimate the parameters V and λ from the first two moments of the velocity profiles (see Materials and Methods), and deduce values of the hydrodynamic screening lengths $L_\eta^{\mathrm{Ras}} = 320 \pm 110\,\mu$m and $L_\eta^{\mathrm{wt}} = 290 \pm 110\,\mu$m (SD, $n = 13$) (Fig. 4,c) that are large compared to the traction force correlation lengths (Fig. 5,d). Finally, we find that the front velocity of transformed monolayers is similar to that of normal ones: $v_{\mathrm{front}}^{\mathrm{Ras}} = 9.9 \pm 3\,\mu\mathrm{m\,h^{-1}}$ and $v_{\mathrm{front}}^{\mathrm{wt}} = 8.7 \pm 3\,\mu\mathrm{m\,h^{-1}}$ (SD, $n = 13$) (Fig. 4,b). Note that the velocity amplitudes obtained by PIV are reduced by a factor of 2 compared to the estimates obtained from front displacements, which may be due to uncertainties of PIV techniques applied close to a free boundary with a time-dependent fluctuating shape[24].

3.4 After contact, the normal monolayer moves backwards

After the gap closes, the migration does not come to a halt and a competition for space arises between the two populations. The Ras monolayer continues to advance, while the wt population moves backwards. Although the details of the movements of the interface may vary from experiment to experiments, we always observe the same direction of interface motion. Close to the interface, some cells from each population locally penetrate the oppo-

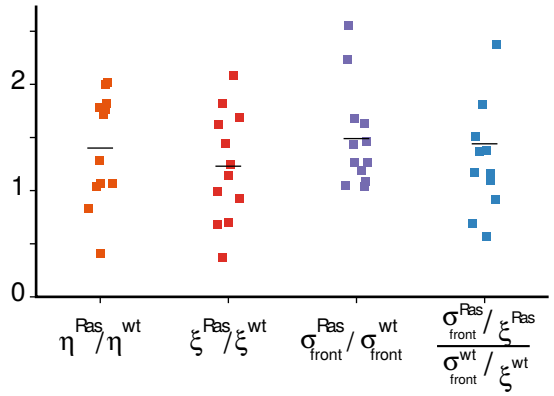

Fig. 6 Relative material parameters for the two competing monolayers From left to right, we show the relative shear viscosity 1.4 ± 0.5, the relative friction coefficient 1.2 ± 0.5, the relative front stress 1.5 ± 0.5 (Eq. (20)) and the relative ratio between front stress and friction coefficient 1.4 ± 0.7 (SD, $n = 12$). Horizontal black lines correspond to mean values.

site one, but the two populations essentially remain separated after fusion, thus forming a visible boundary between the two populations (Fig. 2). To quantify the backward migration of the wt population, we measured the displacement $d_{\text{interface}}$ of the interface separating the two populations during $\Delta t = 30$ h after contact. We found $d_{\text{interface}} = 83 \pm 50\,\mu$m (SD, $n = 13$) with a variation range from a few micrometers (almost static interface) to values larger than $100\,\mu$m. The speed of the interface $v_{\text{interface}} = d_{\text{interface}}/\Delta t$ was deduced from this displacement, $v_{\text{interface}} = 2.7 \pm 1.7\,\mu\text{m h}^{-1}$ (Fig. 3,b).

3.5 Estimation of the relative material parameters

The measurement of $v_{\text{interface}}$ allows us to estimate the relative values of the material parameters of transformed and normal cell monolayers in the light of the theoretical framework given by Eqs. (11-13) (Fig. 6). We use the values of v_{front} obtained from monolayer displacements, instead of the PIV values. We checked that the fitting parameter λ remained constant for times $t_{\text{contact}} \le t \le t_{\text{contact}} + 2$ h (in agreement with the model hypothesis) whereas V decreased as expected towards $v_{\text{interface}}$ (Fig. S5).

First, we use Eq. (18) to obtain the ratio between the viscosities: $\eta^{\text{Ras}}/\eta^{\text{wt}} = 1.4 \pm 0.5$ (SD, $n = 12$). Given the hydrodynamic lengths L_η^{wt}, L_η^{Ras}, Eq. (9), we next deduce the friction coefficients $\xi^{\text{Ras}}/\xi^{\text{wt}} = 1.2 \pm 0.5$ (SD, $n = 12$). By combining these results with Eq. (20), we estimate the ratio of the collective stresses at the front for both monolayers: $\sigma^{\text{Ras}}_{\text{front}}/\sigma^{\text{wt}}_{\text{front}} = 1.5 \pm 0.5$ (SD, $n = 12$). In this sense, Ras-transformed cells are collectively stronger than normal cells. We conclude that the competition between the two cell populations can be framed as the dynamics of a moving interface between two compressible fluids with different front stresses.

4 Discussion

We interpret velocity measurements in antagonistic migration assays (AMAs) between wild type and Ras-transformed HEK cell sheets in the framework of a model in which the monolayers are considered as compressible and active materials with different material parameters. Our analysis shows that collectively, transformed cells are characterized by a larger hydrodynamic length L_η, viscosity η, and cell-substrate friction coefficient ξ than normal cells. Our model predicts that the direction of front migration is determined by the collective forces that build up at the fronts (σ_{front}), rather than by the traction force amplitude (T_0).

Indeed, the average traction force amplitudes of both isolated cells and homogeneous monolayers are larger for normal than for transformed cells. Although large variations of front and interface positions make it hard to directly estimate σ_{front} from the traction force data, we find that the ratio of the average component of traction forces parallel to the direction of migration is consistent with 1, $|\langle T_x \rangle^{\text{Ras}}|/|\langle T_x \rangle^{\text{wt}}| = 0.94 \pm 0.17$, whereas the traction force correlation length is significantly larger in the transformed monolayer compared to the wild type one, $l_f^{\text{Ras}}/l_f^{\text{wt}} = 1.15 \pm 0.18$ (SD, $n = 4$). In this sense, Ras-transformed cells may collectively exert stronger front stresses than normal cells, $\sigma^{\text{Ras}}_{\text{front}} > \sigma^{\text{wt}}_{\text{front}}$. We emphasize that, at the single cell level, Ras cells exhibit lower traction force amplitudes (Fig. S2), whereas at the multicellular level both cell types exhibit forces of similar amplitude in bulk (Fig. S3). Determining how the collective mechanical properties of a cell assembly emerge from individual cell properties and cell-cell interactions remains an essential, but largely unsolved question.

Further, we verified that the ratio $(\sigma_{\text{front}}/\xi)^{\text{Ras}}/(\sigma_{\text{front}}/\xi)^{\text{wt}} = 1.4 \pm 0.7$ (SD, $n = 12$) (Fig. 6) is larger than 1, as already found in the analysis of the kinematics of disk-shaped wound-healing assays with the same cell lines[31]. The quantitative discrepancy between the two (model-dependent) estimates of $(\sigma_{\text{front}}/\xi)^{\text{Ras}}/(\sigma_{\text{front}}/\xi)^{\text{wt}}$ may arise due to different model hypotheses, as the monolayer flow was assumed to be inviscid and incompressible in our previous work[31].

Interestingly, AMAs between normal and Ras^{V12} MDCK cells[12] show the opposite result (Ras MDCK cells being displaced backwards, while normal MDCK cells continue to migrate forward). In this work, the authors concluded that MDCK-Ras cells repulsion by normal MDCK cells is a process that is dependent on E-cadherin-based cell-cell adhesion. In the present study, however, immunostaining for E-cadherin revealed the absence of this protein at the cell-cell junctions for both normal and Ras-transformed HEK cells (Fig. S6). Since E-cadherin is required for EphA2 receptor localization at cell-cell contacts[32,33], Eph receptor signaling cannot be directly involved in our system. On the basis of the present analysis, we conjecture that collective stresses are stronger in MDCK wt cell sheets compared to MDCK Ras cell sheets. Irrespective of the cell line, the connection between molecular constituents and their respective expression levels in normal and transformed cells on the one hand, and the respective hydrodynamic parameter values on the other hand, remains unknown and deserves further study.

In our theoretical framework we have omitted several effects that might be relevant for AMAs, like specific molecular interactions between the two cell populations or changes of cell polarity after contact. Indeed, cell behavior is known to be influenced by the local micro-environment, and thus leading cells may actively change their orientation and repolarize upon fusion with

the competing tissue. If confirmed by observation, this effect could be taken into account by changing accordingly the boundary conditions for the polarity fields Eqs. (14), which would lead to $v_{\rm front}$ being weighted differently in Eq. (18), and to different values of the model-dependent relative parameters. Over longer time scales, tissue material parameters may become time-dependent[20,34], and differences in cell proliferation rates may become relevant[15]. Since we focused here on the vicinity of the contact time between the two populations, we defer to future work the incorporation of these additional ingredients into our theoretical framework.

Our analysis illustrates that AMAs can be used to estimate relative hydrodynamic parameters of spreading monolayers from their kinematics only. We believe that this setting is a useful testing ground to explore the mechanisms governing competition between cellular assemblies.

Conflicts of interest

There are no conflicts to declare.

Acknowledgements

We thank V. Hakim and the members of the team "Biology-inspired physics at mesoscales" for fruitful discussions. The authors belong to the CNRS research consortium (GdR) 'CellTiss'. This work was funded by La Ligue (Équipe labellisée), the Labex CelTisPhyBio, the GEFLUC Ile-de-France and the C'Nano Ile-de-France (projet COMPCELL). SM was supported by a doctoral fellowship from the IPGG, KS by a FPGG grant, and TM was funded by Ecole de l'INSERM.

5 Appendix A

In this Appendix, we solve the evolution equations (1-3) with the boundary conditions:

$$v(x=L) = 0, \tag{21}$$

$$p(x=L) = +1, \tag{22}$$

valid when a single cell sheet located in the fixed domain $x < L$ is clamped at position $x = L$. The polarity profile is unchanged, see Eq. (6). However the velocity and stress profiles now read:

$$v(x) = \frac{v_{\rm front} L_c}{L_c - L_\eta}\left(\exp\left(\frac{x-L}{L_c}\right) - \exp\left(\frac{x-L}{L_\eta}\right)\right), \tag{23}$$

$$\sigma(x) = \frac{\eta v_{\rm front} L_c}{L_c - L_\eta}\left(\frac{1}{L_c}\exp\left(\frac{x-L}{L_c}\right) - \frac{1}{L_\eta}\exp\left(\frac{x-L}{L_\eta}\right)\right). \tag{24}$$

The maximal stress is applied by the monolayer at the front, with $\sigma_{\rm front} = -\sigma(x = L, t)$ given by (20).

Notes and references

1 S. de Beco, M. Ziosi and L. A. Johnston, *Dev Dyn*, 2012, **241**, 831–841.

2 R. Levayer and E. Moreno, *J Cell Biol*, 2013, **200**, 689âĂŞ98.

3 M. Amoyel and E. A. Bach, *Development*, 2014, **141**, 988–1000.

4 M. M. Merino, R. Levayer and E. Moreno, *Tr Cell Biol*, 2016, **26**, 776–788.

5 T. Eichenlaub, S. Cohen and H. Herranz, *Current Biology*, 2016, **26**, 419–427.

6 E. Moreno and K. Basler, *Cell*, 2004, **117**, 117–129.

7 C. Hogan, S. Dupré-Crochet, M. Norman, M. Kajita, C. Zimmermann, A. E. Pelling, E. Piddini, L. A. Baena-López, J.-P. Vincent, Y. Itoh, H. Hosoya, F. Pichaud and Y. Fujita, *Nat Cell Biol*, 2009, **11**, 460–467.

8 C. Gullekson, G. Cojoc, M. Schürmann, J. Guck and A. Pelling, *Soft Matter*, 2017, **13**, 8483–8491.

9 L. Wagstaff, M. Goschorska, K. Kozyrska, G. Duclos, I. Kucinski, A. Chessel, L. Hampton-O'Neil, C. R. Bradshaw, G. E. Allen, E. L. Rawlins, P. Silberzan, R. E. C. Salas and E. Piddini, *Nat Comm*, 2016, **7**, 11373.

10 M. Norman, K. A. Wisniewska, K. Lawrenson, P. Garcia-Miranda, M. Tada, M. Kajita, H. Mano, S. Ishikawa, M. Ikegawa, T. Shimada and Y. Fujita, *J Cell Sci*, 2012, **125**, 59–66.

11 K. D. Nnetu, M. Knorr, J. Käs and M. Zink, *New J Phys*, 2012, **14**, 115012.

12 S. Porazinski, J. de Navascués, Y. Yako, W. Hill, M. R. Jones, R. Maddison, Y. Fujita and C. Hogan, *Current Biology*, 2016, **26**, 3220–3229.

13 H. B. Taylor, A. Khuong, Z. Wu, Q. Xu, R. Morley, L. Gregory, A. Poliakov, W. R. Taylor and D. G. Wilkinson, *J Roy Soc Interface*, 2017, **14**, 20170338.

14 Rodríguez-Franco, Pilar, Brugués, Agustí, A. Marín-Llauradó, V. Conte, G. Solanas, E. Batlle, J. J. Fredberg, P. Roca-Cusachs, R. Sunyer and X. Trepat, *Nat Mat*, 2017, **16**, 1029–1037.

15 J. Ranft, M. Aliee, J. Prost, F. Jülicher and J.-F. Joanny, *New J Phys*, 2014, **16**, 035002.

16 T. Lorenzi, A. Lorz and B. Perthame, *Kinetic Rel Mod*, 2016, **10**, 299–311.

17 A. Hallou, J. Jennings and A. J. Kabla, *Roy Soc Open Sci*, 2017, **4**, 161007.

18 S. Nishikawa, A. Takamatsu, S. Ohsawa and T. Igaki, *J Theor Biol*, 2016, 40–50.

19 M. Poujade, E. Grasland-Mongrain, A. Hertzog, J. Jouanneau, P. Chavrier, B. Ladoux, A. Buguin and P. Silberzan, *Proc Natl Acad Sci U S A*, 2007, **104**, 15988–15993.

20 C. Blanch-Mercader, R. Vincent, E. Bazellières, X. Serra-Picamal, X. Trepat and J. Casademunt, *Soft Matter*, 2017, **13**, 1235–1243.

21 W. C. Hahn, C. M. Counter, A. S. Lundberg, R. L. Beijersbergen, M. W. Brooks and R. A. Weinberg, *Nature*, 1999, **400**, 464–468.

22 W. Rasband, *ImageJ v1.46b*, US Natl Inst Health, Bethesda, MD technical report, 2012.

23 L. Petitjean, M. Reffay, E. Grasland-Mongrain, M. Poujade, B. Ladoux, A. Buguin and P. Silberzan, *Biophys J*, 2010, **98**, 1790–1800.

24 M. Deforet, M. C. Parrini, L. Petitjean, M. Biondini, A. Buguin, J. Camonis and P. Silberzan, *Nat Methods*, 2012, **9**, 1081–

1083.
25 J. R. Tse and A. J. Engler, *Curr Protocols Cell Biol*, 2010, **47**, 10.16.1–10.16.16.
26 A. Azioune, N. Carpi, Q. Tseng, M. Théry and M. Piel, *Methods Cell Biol*, 2010, **97**, 133–146.
27 J.-L. Martiel, A. Leal, L. Kurzawa, M. Balland, I. Wang, T. Vignaud, Q. Tseng and M. Théry, *Methods Cell Biol*, 2015, **125**, 269–287.
28 J. P. Butler, I. M. Tolić-Norrelykke, B. Fabry and J. J. Fredberg, *Am J Physiol Cell Physiol*, 2002, **282**, C595–C605.
29 S. Munevar, Y. li Wang and M. Dembo, *Biophys J*, 2001, **80**, 1744–1757.
30 X. Trepat, M. R. Wasserman, T. E. Angelini, E. Millet, D. A. Weitz, J. P. Butler and J. J. Fredberg, *Nat Phys*, 2009, **5**, 426–430.
31 O. Cochet-Escartin, J. Ranft, P. Silberzan and P. Marcq, *Biophys J*, 2014, **106**, 65–73.
32 N. D. Zantek, M. Azimi, M. Fedor-Chaiken, B. Wang, R. Brackenbury and M. S. Kinch, *Cell Growth Differ*, 1999, **10**, 629–638.
33 S. Orsulic and R. Kemler, *J Cell Sci*, 2000, **113**, 1793–1802.
34 S. Garcia, E. Hannezo, J. Elgeti, J.-F. Joanny, P. Silberzan and N. S. Gov, *Proc Natl Acad Sci U S A*, 2015, **112**, 15314–15319.